Article

Evidence for unconventional superconductivity in twisted trilayer graphene

https://doi.org/10.1038/s41586-022-04715-z

Received: 20 September 2021

Accepted: 1 April 2022

Published online: 15 June 2022

Check for updates

Hyunjin Kim[1,2,3,7], Youngjoon Choi[1,2,3,7], Cyprian Lewandowski[2,3,4], Alex Thomson[2,3,4,5], Yiran Zhang[1,2,3], Robert Polski[1,2], Kenji Watanabe[6], Takashi Taniguchi[6], Jason Alicea[2,3,4] & Stevan Nadj-Perge[1,2]✉

Magic-angle twisted trilayer graphene (MATTG) has emerged as a moiré material that exhibits strong electronic correlations and unconventional superconductivity[1,2]. However, local spectroscopic studies of this system are still lacking. Here we perform high-resolution scanning tunnelling microscopy and spectroscopy of MATTG that reveal extensive regions of atomic reconstruction favouring mirror-symmetric stacking. In these regions, we observe symmetry-breaking electronic transitions and doping-dependent band-structure deformations similar to those in magic-angle bilayers, as expected theoretically given the commonality of flat bands[3,4]. Most notably in a density window spanning two to three holes per moiré unit cell, the spectroscopic signatures of superconductivity are manifest as pronounced dips in the tunnelling conductance at the Fermi level accompanied by coherence peaks that become gradually suppressed at elevated temperatures and magnetic fields. The observed evolution of the conductance with doping is consistent with a gate-tunable transition from a gapped superconductor to a nodal superconductor, which is theoretically compatible with a sharp transition from a Bardeen–Cooper–Schrieffer superconductor to a Bose–Einstein-condensation superconductor with a nodal order parameter. Within this doping window, we also detect peak–dip–hump structures that suggest that superconductivity is driven by strong coupling to bosonic modes of MATTG. Our results will enable further understanding of superconductivity and correlated states in graphene-based moiré structures beyond twisted bilayers[5].

Figure 1a–c shows a schematic of the scanning tunnelling microscopy (STM) setup and the magic-angle twisted trilayer graphene (MATTG) topography formed by alternately rotating three graphene layers by a twist angle $\theta = 1.5°$ (refs. [1–3]), resulting in a moiré wavelength of $L_M = a/(2\sin(\theta/2)) \approx 9$ nm, where $a = 0.246$ nm is the graphene crystal lattice (see Methods for fabrication and measurement details). As MATTG is composed of three layers, two independent moiré patterns can in principle arise and, moreover, possible offsets between the first and third layers could result in even more complex outcomes. Notably, however, we consistently observe a unique triangular moiré lattice, with no sign of an additional underlying moiré pattern, signalling the formation of a single predominantly A–tw–A configuration in which the first and third layers are aligned and the second layer is twisted by θ (Fig. 1c, d). This observation suggests that mirror symmetric A–tw–A stacking is preferred, in line with previous ab initio theory calculations[6] and transport measurements[1,2]. In addition, in large-scale topographies, we occasionally observe stripe-like features (Fig. 1b) that are not reported in twisted bilayers. We attribute these stripes to domain boundaries where strain in the top and bottom layers arises as a result of the atomic reconstruction necessary to maintain the A–tw–A stacking across the domains (Fig. 1e, Supplementary Information 2).

Spectroscopy of MATTG (Fig. 1f) upon electrostatic doping (controlled by the gate voltage V_{Gate}) is similar to magic-angle twisted bilayer graphene (MATBG) in many respects—a reflection of the alternating-angle stacking of the trilayer, which conspires to form spin–valley-degenerate flat bands, together with additional dispersive Dirac cones[3,6]. The two Van Hove singularities (VHSs) originating from those flat bands, detected as peaks in tunnelling conductance dI/dV (where dI is the change tunnelling current upon change dV in bias voltage V_{Bias}), are pushed apart at the charge neutrality point (CNP, $\nu = 0$) compared with full filling of four electrons (holes) per moiré unit cell (filling factor $\nu = \pm 4$). The approximately fivefold change in VHS separation indicates that the partially filled flat-band structure is largely determined by electronic correlations in analogy with the behaviour seen in MATBG[7–10]. A well developed cascade of flavour-symmetry-breaking phase transitions[11,12] is also observed (Fig. 1f). The overall spectroscopic similarities between MATTG and

[1]T. J. Watson Laboratory of Applied Physics, California Institute of Technology, Pasadena, CA, USA. [2]Institute for Quantum Information and Matter, California Institute of Technology, Pasadena, CA, USA. [3]Department of Physics, California Institute of Technology, Pasadena, CA, USA. [4]Walter Burke Institute for Theoretical Physics, California Institute of Technology, Pasadena, CA, USA. [5]Department of Physics, University of California, Davis, Davis, CA, USA. [6]National Institute for Materials Science, Tsukuba, Japan. [7]These authors contributed equally: Hyunjin Kim, Youngjoon Choi. ✉e-mail: s.nadj-perge@caltech.edu

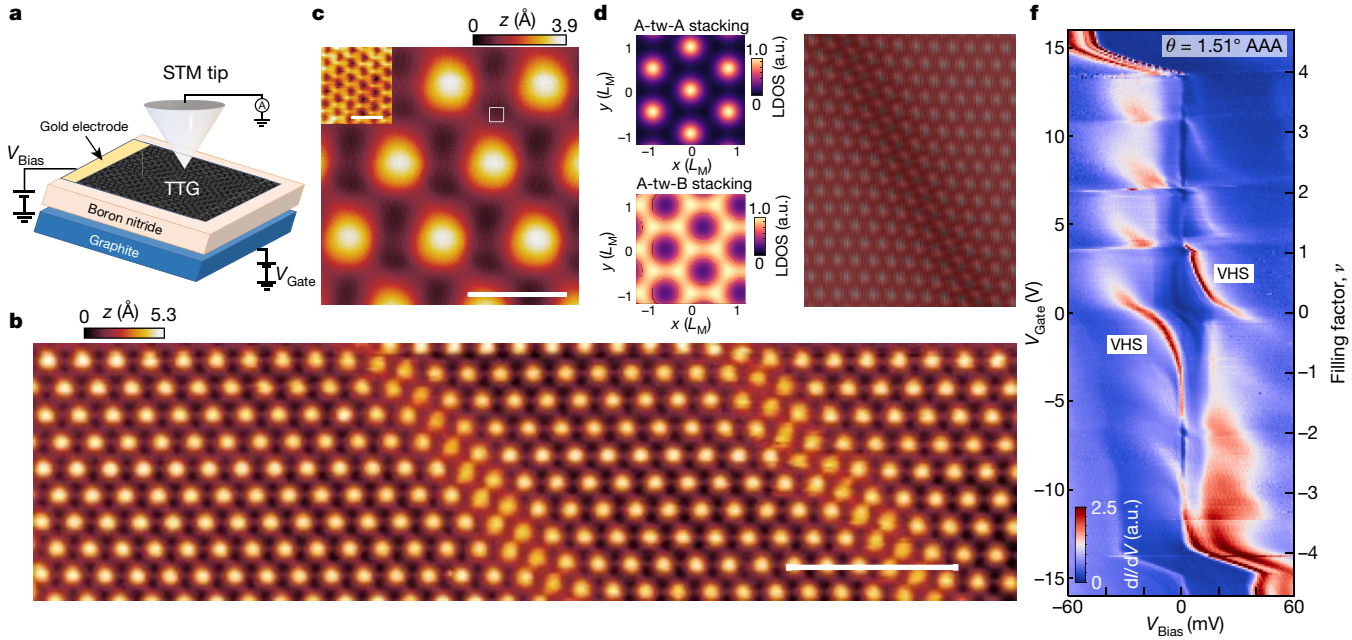

Fig. 1 | Topography and spectroscopy of MATTG at zero magnetic field. **a**, Schematic of the STM experiment. MATTG is placed on a hexagonal boron nitride substrate and the doping is controlled by a graphite back gate. **b**, A topography (height, z) of a 290 nm by 80 nm area where two stripes separated by approximately 100 nm are observed (tunnelling set point parameters: V_{Bias} = 100 mV and I = 20 pA). Scale bar, 50 nm. **c**, A 26 nm by 26 nm topography showing moiré lattices with corresponding moiré length of approximately 9 nm. Scale bar, 10 nm. Inset: the atomic-scale hexagonal lattice of carbon atoms. Scale bar, 0.5 nm. **d**, Calculated LDOS at charge neutrality originating from the bands within approximately ±50 meV energy window for A–tw–A (top) and A–tw–B (bottom) stacking. Although, in principle, various configurations could arise, the A–tw–A stacking, where the first and third layers are aligned, is seen experimentally. The peaks in LDOS correspond to AAA stacked regions where carbon atoms from three graphene layers are aligned. **e**, Simulated atomic distribution of MATTG with the first and third layers strained with respect to each other (see Supplementary Information 2 for simulation details). **f**, Tunnelling conductance (dI/dV) spectroscopy as a function of V_{Gate} at a twist angle θ = 1.51° on an AAA site at T = 400 mK. Clear signatures of symmetry breaking cascades, similar to twisted graphene bilayers[12,13], are observed.

MATBG suggest that the flat bands in MATTG dominate the local density of states (LDOS) in this regime. We do nevertheless detect subtle signatures of the expected additional Dirac cones. Most obviously, contrary to twisted bilayers, at $\nu = \pm 4$ the LDOS is neither completely suppressed nor accompanied by quantum-dot formation[13] (Extended Data Fig. 1)—indicating the presence of gapless states intervening between the flat bands and remote dispersive bands.

The LDOS at the Fermi level measured at finite magnetic fields[13] provides further signatures of the additional Dirac cones in MATTG (Fig. 2a). We resolve clear Landau fans emanating from zero field around $\nu = 0, \pm 4$ along with $\nu = \pm 1, \pm 2$; the latter signal Fermi surface reconstructions are due to flavour-symmetry-breaking transitions, in agreement with transport studies[1,2]. The main fan sequence originating from $\nu = +4$ is +2, +6, ... (−2, −6, ... for $\nu = -4$) instead of the 0, +4, ... pattern typically seen in MATBG devices. The relative Chern-number shift of 2 arises from the zeroth Landau level (LL) associated with the additional Dirac cones, which contribute to the total Chern number at $\nu = \pm 4$. Finite-bias spectroscopy in magnetic fields more directly exposes the presence of additional Dirac cones in the spectrum (Fig. 2c, d) and filling-dependent band-structure renormalization[14,15], arising owing to non-uniform charge distribution as observed in twisted bilayers[16] (see also Extended Data Figs. 2, 3, Methods, Supplementary Information 3 for more details). We can clearly identify the $N = 0, \pm 1, \pm 2, \ldots$ LLs originating from the Dirac dispersion; the increase of LL separation with field (Fig. 2i) confirms the linear dispersion and yields a monolayer-graphene Dirac velocity in agreement with theoretical expectations[4,6]. Moreover, the calculated density of states, taking into account the band-structure renormalization of the flat bands (Fig. 2b), is in a good agreement with the experiment (Fig. 2e–h).

Superconductivity near $\nu = -2$

Having established the foundational properties of the MATTG band structure, we now turn to the doping range $-3 \lesssim \nu \lesssim -2$, where significant suppression of the tunnelling conductance is observed (Fig. 3a). This feature is primarily observed in two regions—one at $-2.1 < \nu < -1.9$ and the other at $-3 < \nu < -2.2$. The former interval, around $\nu \approx -2$, exhibits a correlation-induced gap accompanied by Coulomb diamonds and nearly horizontal resonance peaks, signalling the formation of quantum dots and a correlated insulating state[13,17], despite the presence of the additional Dirac cones.

Throughout the second interval, $-3 < \nu < -2.2$, the tunnelling conductance minimum is well pinned to the Fermi energy ($V_{Bias} = 0$) despite the large change in filling. Notably, this suppression is accompanied by peak structures symmetrically placed around the Fermi energy as the line traces show in Fig. 3b, c (it is noted that the spectra taken at $-2.1 < \nu < -1.9$ or at around other filling factors do not exhibit these symmetric peaks; Extended Data Figs. 4, 5). The presence of such sharp narrow peaks—which strongly resemble coherence peaks in superconductors and occur in the filling range where transport experiments observe superconductivity[1,2]—is the first indication that this spectroscopic signature arises from superconductivity in MATTG. The superconductivity in our samples is independently confirmed by the point contact spectroscopy measurements that reveal the presence of an Andreev reflection process around the same filling range (Methods, Extended Data Fig. 6).

The temperature and magnetic field dependence of the tunnelling spectra (Fig. 3d–g) and the observed coherence peaks further point to its superconducting origin while also establishing its unconventional nature. As the temperature is increased, the coherence peaks on both sides of the Fermi energy subside gradually until 2–2.5 K (close to the maximum critical temperature reported in transport[1]), where the

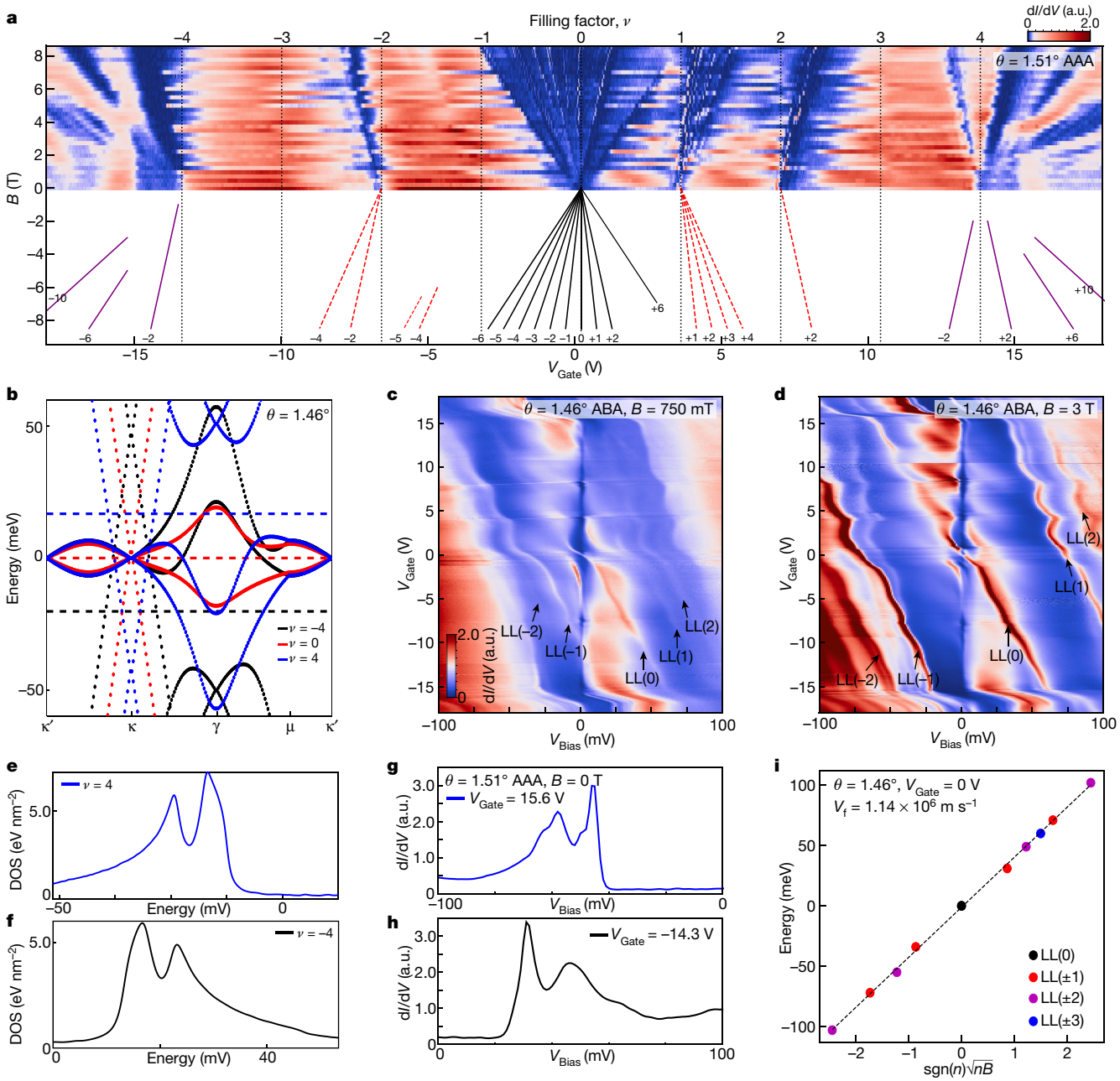

Fig. 2 | LDOS Landau fan diagram and doping-dependent band deformations in MATTG. a, LDOS Landau fan diagram[13] measured on an AAA site. The negative magnetic field fan shows the corresponding schematic of gaps between LLs emanating from the CNP (black); gaps emanating from non-zero integer fillings (red); and gaps between LLs from the dispersive bands (purple). **b**, Calculated MATTG band structure taking into account Hartree corrections. The horizontal dashed lines represent the positions of the Fermi levels at each doping. Electron (hole) doping shifts the Dirac-like band towards negative (positive) energy relative to the flat band (Supplementary Information 3). **c**, **d**, Point spectroscopy on an ABA site (in between AAA sites) at finite magnetic fields $B = 750$ mT (**c**) and $B = 3$ T (**d**). The black arrows indicate LLs identified to originate from the additional Dirac cones characteristic of MATTG. **e**, **f**, Calculated density of states with Hartree corrections at $\nu = 4$ (**e**) and $\nu = -4$ (**f**) for $\theta = 1.51°$ at $B = 0$ T. **g**, **h**, Point spectra taken at an AAA site at $B = 0$ T near $\nu = 4$ ($V_{Gate} = 15.6$ V; **g**) and $\nu = -4$ ($V_{Gate} = -14.3$ V; **h**). Note the asymmetric profile as expected from **e**, **f**. **i**, Energies of LLs extracted from **c**, **d** at $V_{Gate} = 0$ V and plotted versus $\mathrm{sgn}(n)\sqrt{|n|B}$, where n is the LL index, showing agreement with expectations from a Dirac dispersion and the value of graphene Fermi velocity V_f. All data in this figure are taken within a 100×100 nm^2 MATTG area with average $\theta = 1.48 \pm 0.03°$. The angles shown in the panels are obtained from measuring the exact distances between the closest AAA sites. Measurements are taken at $T = 2$ K.

hole-side peak completely disappears (Fig. 3d, f) and the zero-bias conductance exhibits a visible upturn (Fig. 3e; see also Extended Data Fig. 7 for more data). Suppressed zero-bias conductance together with a significantly broadened electron-side peak nevertheless survives at this temperature; both features are washed out only around $T^* \approx 7$ K (Fig. 3e, f). Persistent conductance suppression beyond the disappearance of coherence peaks is typically interpreted as evidence of a pseudogap phase with higher transition temperature linked to T^* characteristic of unconventional superconductors such as cuprates or thin films of disordered alloys[18,19] (see Extended Data Fig. 8 for data near $\nu = +2$). Our observation of two different temperature scales is consistent with the existence of superconducting and pseudogap phases in MATTG. In any case, the gradual disappearance of the coherence peaks with temperature reaffirms its superconducting origin.

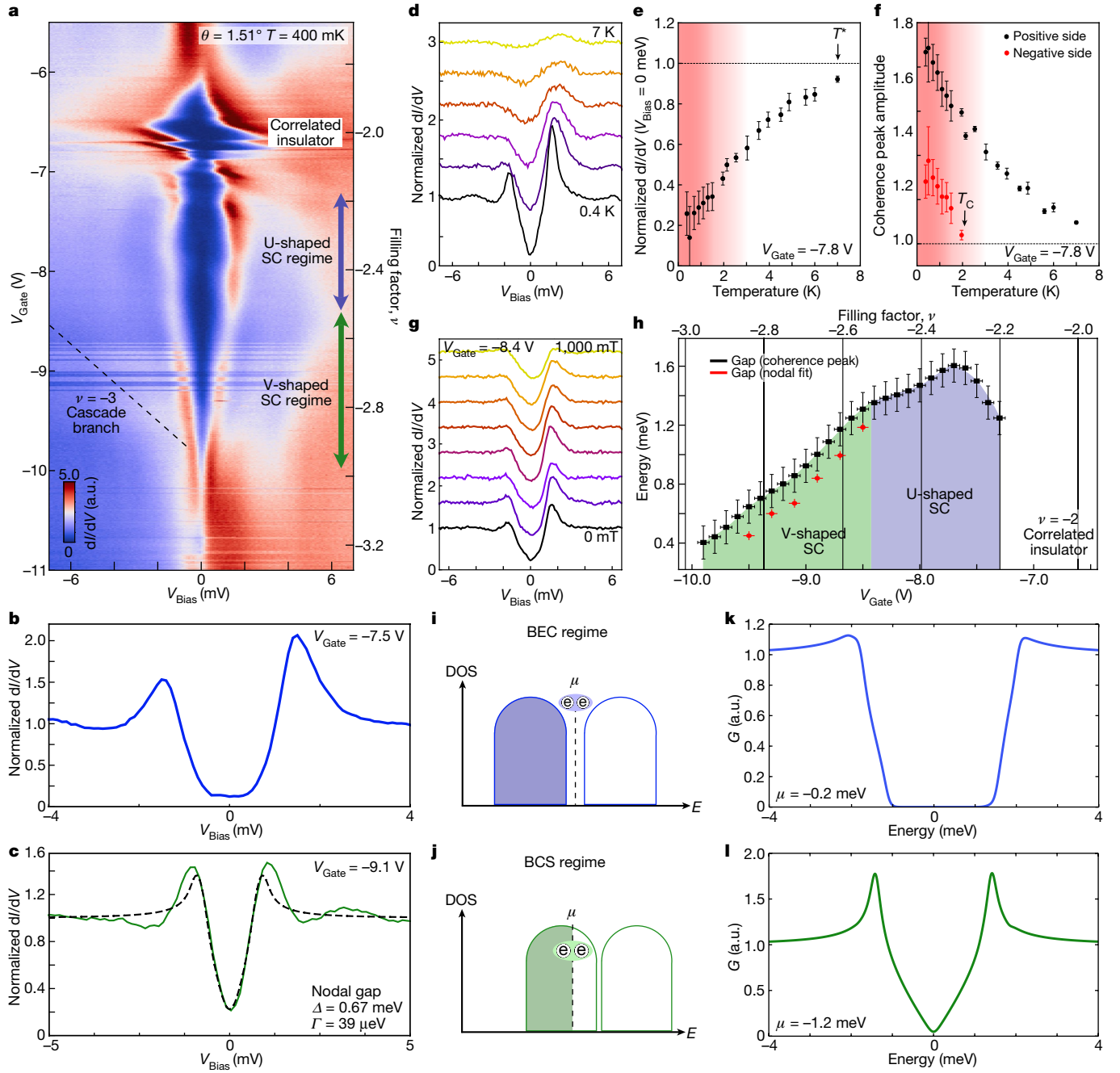

Fig. 3 | Spectroscopic gap in the −3 < ν < −2 range and signatures of unconventional superconductivity. a, Spectra near an AAA site (same area as Fig. 2a). The purple and green arrows denote the ν range over which the U-shaped and V-shaped tunnelling spectra, accompanied by clear coherence peaks, are observed. **b**, **c**, Normalized spectra showing U-shaped (**b**) and V-shaped (**c**) tunnelling suppression. The data are normalized by a polynomial background, and fit to the Dynes formula (**c**) with a nodal superconducting order parameter (Supplementary Information 4). **d**, Temperature dependence of the spectrum (lines correspond to T = 0.4 K, T = 2 K, T = 3 K, T = 4.5 K, T = 5.6 K and T = 7 K). **e**, Normalized zero-bias conductance versus temperature. T^* indicates the temperature at which the zero-bias conductance reaches 90% of the conductance outside the gap. **f**, Coherence-peak amplitude versus temperature from normalized spectra on the electron (black) and hole (red) side. The hole-side coherence peak gets fully suppressed around $T_C \approx 2$–2.5 K. Panels **d**–**f** are from the same dataset as Extended Data Fig. 7h–k. **g**, Magnetic-field dependence of the spectrum (lines correspond to B = 0 mT, B = 100 mT, B = 200 mT, B = 300 mT, B = 400 mT, B = 600 mT, B = 800 mT and B = 1,000 mT), from the same dataset as Extended Data Fig. 7a–d. **h**, Gap size Δ versus ν (V_{Gate}) extracted from **a** half of a separation between coherence peaks. The red markers indicate the gap size extracted from the nodal gap fit. Error bars are set by the experimental resolution (0.1 meV) and standard error of the fits. The colour coding of different regions matches **a**. **i**–**l**, Proposed transition from BEC (**i**) to BCS (**j**) regime that qualitatively reproduces the U-shaped and V-shaped spectra showing conductance G (**k**, **l**); see main text, Supplementary Information 5B, Supplementary Fig. 6.

Denoting the coherence peak-to-coherence peak distance as 2Δ, we find maximal $\Delta \approx 1.6$ meV near $\nu = -2.4$ (Fig. 3h). The overall doping dependence of the spectroscopic gap resembles the doping dependence of the critical temperature T_C (refs. [1,2]), which also peaks around $\nu \approx -2.4$, suggesting a correlation between these two quantities. The maximum critical temperature $T_C \approx 2$–2.5 K from transport[1] yields a ratio $2\Delta/k_B T_C \approx 15$–19 (where k_B is the Boltzmann constant) that far exceeds the conventional Bardeen–Cooper–Schrieffer (BCS)

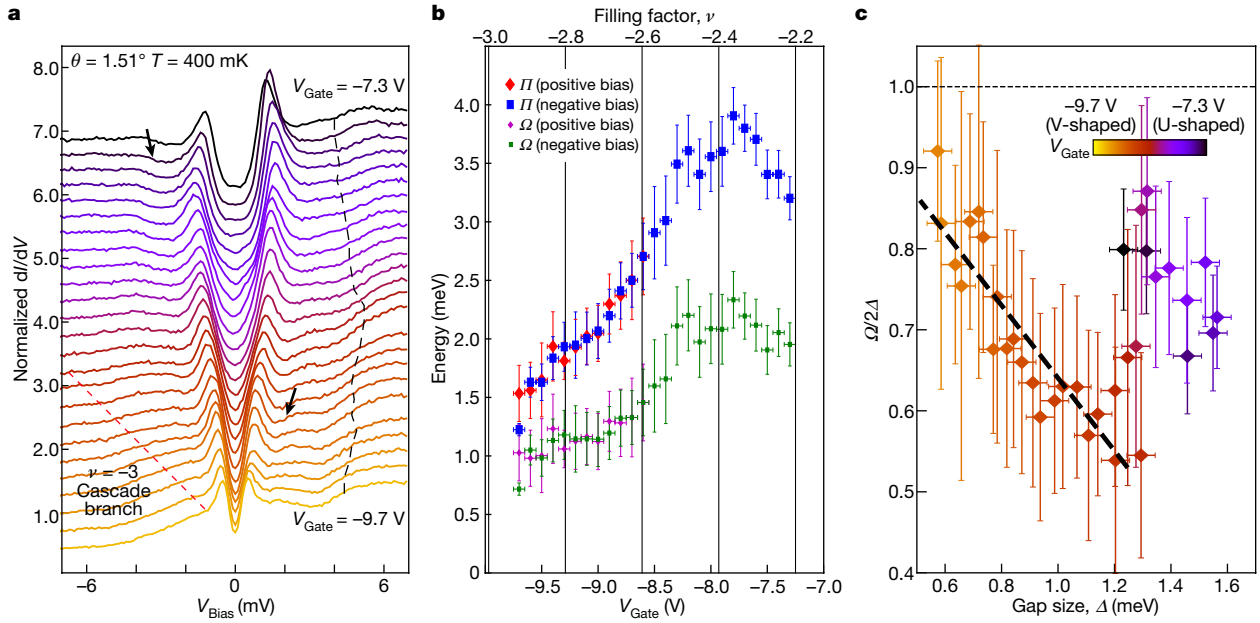

Fig. 4 | Peak–dip–hump structure in MATTG. a, Line traces showing point spectra for V_{Gate} ranging from −9.7 V to −7.3 V (same dataset as Fig. 3a). Each spectrum is divided by the mean value for clarity. The red dashed line indicates the LDOS peak originating from the subband that abruptly shifts owing to the cascade near $\nu = -3$; the black dashed line indicates the shoulder of the upper flat band VHS. The black arrows denote the position of hole-side and electron-side dip–hump structure identified from the local minimum and maximum in d^2I/dV^2. **b**, Extracted energy Π of the electron-side (red) and hole-side (blue) dip–hump structure and corresponding energy Ω of the bosonic mode on the electron side (purple) and hole side (green) versus filling factor (V_{Gate}). Error bars are set by the full-width at half-maximum of the d^2I/dV^2 signal. **c**, Ratio $\Omega/2\Delta$ plotted versus Δ for both electron-side and hole-side bosonic excitations. The black dashed line is a linear regression of the data at V_{Gate} ranging from −9.7 V to −8.6 V that shows anticorrelation of the two quantities for fillings at which V-shaped tunnelling spectra are observed. Error bars are propagated from errors in determining Ω (as in **b**) and experimental resolution determining error of Δ.

value (about 3.5)—highlighting the strong-coupling nature of superconductivity in MATTG. We note that in the V-shaped regime, nodal fits give a 10–30% smaller value of Δ compared with the estimate from the coherence-peak-to-coherence-peak distance. Even using this estimate $2\Delta/k_BT_C \approx 10$ is still much larger than the expectation from BCS theory. Also, the measured spectroscopic gaps imply a maximum Pauli limit of about 10 T for the destruction of spin-singlet superconductivity.

The coherence peak height at base temperature ($T = 400$ mK) also gradually decreases with perpendicular magnetic field, similar to tunnelling conductance measurements through MATBG junctions[20]. We observe that the coherence peaks are greatly diminished by 1 T and therefore infer a critical field $B_C \gtrsim 1$ T at $\nu \approx -2.4$ (Fig. 3g; see also Extended Data Fig. 7). This result is compatible with the small Ginzburg–Landau coherence length of $\xi_{GL} \approx 12$ nm reported around optimal doping[1] upon using the naive estimate $B_C \approx \Phi_0/2\pi\xi_{GL}^2 \approx 2$T, where Φ_0 is the magnetic flux quantum. It is noted that the LDOS suppression without coherence peaks persists up to much larger fields (Extended Data Fig. 7f, g).

U-shape-to-V-shape gap transition

Interestingly, suppressed tunnelling conductance within the coherence peaks typically evolves from a U-shaped profile at $-2.4 \lesssim \nu < -2.2$ (Fig. 3b) to a V-shaped profile at $-3 \lesssim \nu \lesssim -2.4$ (Fig. 3c), which suggests that there are two distinct superconducting regimes. The magnetic-field dependence of the tunnelling conductance further distinguishes these regimes: the field more efficiently suppresses the spectroscopic gap in the V-shaped window compared with the U-shaped window (Extended Data Fig. 7). The V-shaped tunnelling spectra resemble that of cuprates and can be well fit using the standard Dynes formula[21] with a pairing order parameter that yields gapless nodal excitations as reported in twisted bilayer graphene[5] (Fig. 3c, Extended Data Figs. 9, 10, Supplementary Information 4). The enhanced conductance suppression of the U-shaped spectra instead suggests the onset of a fully gapped superconducting state (Extended Data Fig. 11). One logical possibility is that the U- and V-shaped regimes admit distinct superconducting order parameter symmetries that underlie a transition from a gapped to gapless paired state on hole doping (similar behaviour has been proposed for cuprates[22]). Finally, it is noted that even in a U-shaped region, a standard isotropic *s*-wave pairing order parameter produces a significantly worse fit relative to fits that assume either a mixture of *s*-wave and nodal order parameters or that use a $d + id$-like order parameter (Supplementary Information 4, Extended Data Fig. 9).

We point here to an alternative explanation whereby the transition from a U-shaped regime to a V-shaped regime can be understood in the context of Bose–Einstein-condensate (BEC) and BCS phases with a single nodal order parameter. In this scenario, starting from the correlation-induced gapped flat bands at $\nu = -2$, hole doping initially introduces BEC-like superconductivity rather than simply depleting the lower flat band; that is, the chemical potential remains within the gap of the correlated insulator (Fig. 3i). This superconducting state can still feature a nodal order parameter while remaining fully gapped as, crucially, the original correlation-induced flat-band gap precludes gapless quasiparticle excitations. Further hole doping eventually begins depleting the lower flat band (Fig. 3j), at which point, the system transitions to a BCS-like superconductor. Here, Cooper pair formation onsets at the Fermi energy, and the nodal order parameter allows for gapless quasiparticle excitations. (When compared against a BEC phase, we use 'BCS' to describe a superconductor for which the chemical potential intersects a band, independent of the pairing mechanism or the coupling strength.) The gapped versus gapless distinction implies that the U-shaped and V-shaped regimes

are separated by a clear transition[23,24] as opposed to the well studied BEC–BCS crossover[25,26] that is operative when both regimes are fully gapped and not topologically distinct.

We phenomenologically model such a transition by considering the tunnelling conductance of a system with electron and hole bands that experience doping-dependent band separation and nodal pairing chosen to mimic experiment; for details see Supplementary Information 5B. In the fully gapped BEC phase, this model yields U-shaped tunnelling spectra (Fig. 3k) that qualitatively match the measured conductance. Indeed, as in experiment, the conductance gap profile does not fit an isotropic *s*-wave pairing amplitude well owing to the additional structure from the nodal order parameter. When the system enters the BCS phase (the chemical potential lies inside the band), the gapless nodal BCS phase instead yields a V-shaped tunnelling profile (Fig. 3l) that also qualitatively matches the experiment. This interpretation of the U-shape-to-V-shape transition is bolstered by transport measurements[1] that reveal two regimes for the Ginzburg–Landau coherence length (Supplementary Information 5B).

Peak–dip–hump structure

Adjacent to the coherence peaks, we observe dip–hump features in the tunnelling conductance that persist over a broad doping range (Fig. 4). The positive and negative voltage dips are typically symmetric in energy, independent of the filling—ruling out the possibility that the dip–hump structure is intrinsic to background density of states. Similar dip–hump features are observed spectroscopically in a range of both conventional strongly coupled phonon superconductors[27,28] as well as unconventional cuprate, iron-based and heavy fermion superconductors[29–34]. Such features are usually interpreted as a signature of bosonic modes that mediate superconductivity and can thus provide key insight into the pairing mechanism[35,36]. If a superconductor exhibits strong electron–boson coupling, dip–hump signatures are expected to appear at energies $\Pi = \Delta + \Omega$, where Δ is the spectroscopic gap defined above and Ω is the bosonic-mode excitation energy[35–37]. We extract the energy of the mode $\Omega = \Pi - \Delta$ as a function of doping (Fig. 4b) and find it to be correlated with Δ. In the V-shaped region, $\Omega/(2\Delta)$ anticorrelates with the spectroscopic gap—in agreement with the trends seen in cuprates and iron-based compounds[29,30,32,33,38]—and is bounded to be less than 1 (Fig. 4c). The upper bound of $\Omega/(2\Delta) \leq 1$ suggests[38–40] that the pairing glue originates from a collective mode related to electronic degrees of freedom, although we cannot rule out low-energy phonons through this line of argument (see Methods for additional discussion). Even if not directly related to the pairing mechanism, dip–hump features anticorrelated with the gap may be valuable signatures of a proximate competing order. Finally, we note that in the U-shaped region, $\Omega/(2\Delta)$ does not exhibit a clear anticorrelation with the spectroscopic gap, possibly owing to subtleties with extracting the true superconducting order parameter in the BEC phase.

Signatures of MATTG superconductivity presented in this work, beyond the observation of Andreev reflection (Extended Data Fig. 6), include: (1) coherence peaks that are suppressed with temperature and magnetic field, but persist well beyond the BCS limit; (2) a pseudogap-like regime; (3) dip–hump structures in the tunnelling conductance; and (4) tunnelling conductance profiles that are not adequately fit with an *s*-wave order parameter, but instead are compatible with a gate-tuned transition from a gapped BEC to a gapless BCS phase with a common nodal order parameter. Comparing with measurements on twisted bilayer graphene[5], it is noted that some of the similarities—including nodal tunnelling spectra, giant gap-to-T_C ratios, and pseudogap physics with anomalous resilience to temperature and magnetic fields—suggest a common origin of superconductivity in bilayers and trilayers. Properties (1)–(3) are typically associated with non-phonon-mediated pairing, although phonon-driven mechanisms can exhibit some of these features (see Methods for additional discussions). Regardless of the pairing-mechanism details, together with property (4), the observed signatures provide unambiguous spectroscopic evidence of the unconventional nature of MATTG superconductivity. Future theories addressing properties (1)–(4) will probably be needed to pinpoint the exact mechanism of superconductivity in this system.

Online content

Any methods, additional references, Nature Research reporting summaries, source data, extended data, supplementary information, acknowledgements, peer review information; details of author contributions and competing interests; and statements of data and code availability are available at https://doi.org/10.1038/s41586-022-04715-z.

1. Park, J. M., Cao, Y., Watanabe, K., Taniguchi, T. & Jarillo-Herrero, P. Tunable strongly coupled superconductivity in magic-angle twisted trilayer graphene. *Nature* **590**, 249–255 (2021).
2. Hao, Z. et al. Electric field–tunable superconductivity in alternating-twist magic-angle trilayer graphene. *Science* **371**, 1133–1138 (2021).
3. Khalaf, E., Kruchkov, A. J., Tarnopolsky, G. & Vishwanath, A. Magic angle hierarchy in twisted graphene multilayers. *Phys. Rev. B* **100**, 085109 (2019).
4. Li, X., Wu, F. & MacDonald, A. H. Electronic structure of single-twist trilayer graphene. Preprint at https://arxiv.org/abs/1907.12338 (2019).
5. Oh, M. et al. Evidence for unconventional superconductivity in twisted bilayer graphene. *Nature* **600**, 240–245 (2021).
6. Carr, S. et al. Ultraheavy and ultrarelativistic dirac quasiparticles in sandwiched graphenes. *Nano Lett.* **20**, 3030–3038 (2020).
7. Kerelsky, A. et al. Maximized electron interactions at the magic angle in twisted bilayer graphene. *Nature* **572**, 95–100 (2019).
8. Choi, Y. et al. Electronic correlations in twisted bilayer graphene near the magic angle. *Nat. Phys.* **15**, 1174–1180 (2019).
9. Xie, Y. et al. Spectroscopic signatures of many-body correlations in magic-angle twisted bilayer graphene. *Nature* **572**, 101–105 (2019).
10. Jiang, Y. et al. Charge order and broken rotational symmetry in magic-angle twisted bilayer graphene. *Nature* **573**, 91–95 (2019).
11. Zondiner, U. et al. Cascade of phase transitions and Dirac revivals in magic-angle graphene. *Nature* **582**, 203–208 (2020).
12. Wong, D. et al. Cascade of electronic transitions in magic-angle twisted bilayer graphene. *Nature* **582**, 198–202 (2020).
13. Choi, Y. et al. Correlation-driven topological phases in magic-angle twisted bilayer graphene. *Nature* **589**, 536–541 (2021).
14. Fischer, A. et al. Unconventional superconductivity in magic-angle twisted trilayer graphene. *npj Quantum Mater.* **7**, 1–10 (2022).
15. Phong, V. T., Pantaleo´n, P. A., Cea, T. & Guinea, F. Band structure and superconductivity in twisted trilayer graphene. *Phys. Rev. B* **104**, L121116 (2021).
16. Choi, Y. et al. Interaction-driven band flattening and correlated phases in twisted bilayer graphene. *Nat. Phys.* **17**, 1375–1381 (2021).
17. Jung, S. et al. Evolution of microscopic localization in graphene in a magnetic field from scattering resonances to quantum dots. *Nat. Phys.* **7**, 245–251 (2011).
18. Eagles, D. M. Possible pairing without superconductivity at low carrier concentrations in bulk and thin-film superconducting semiconductors. *Phys. Rev.* **186**, 456–463 (1969).
19. Renner, C., Revaz, B., Genoud, J.-Y., Kadowaki, K. & Fischer, Ø. Pseudogap precursor of the superconducting gap in under- and overdoped $Bi_2Sr_2CaCu_2O_{8+\delta}$. *Phys. Rev. Lett.* **80**, 149–152 (1998).
20. Rodan-Legrain, D. et al. Highly tunable junctions and non-local Josephson effect in magic-angle graphene tunnelling devices. *Nat. Nanotechnol.* **16**, 769–775 (2021).
21. Dynes, R. C., Narayanamurti, V. & Garno, J. P. Direct measurement of quasiparticle-lifetime broadening in a strong-coupled superconductor. *Phys. Rev. Lett.* **41**, 1509–1512 (1978).
22. Yeh, N.-C. et al. Evidence of doping-dependent pairing symmetry in cuprate superconductors. *Phys. Rev. Lett.* **87**, 087003 (2001).
23. Botelho, S. S. & Sá de Melo, C. A. R. Lifshitz transition in *d*-wave superconductors. *Phys. Rev. B* **71**, 134507 (2005).
24. Borkowski, L. & de Melo, C. S. Evolution from the BCS to the Bose–Einstein limit in a *d*-wave superconductor at *T*=0. *Acta Phys. Pol. A* **6**, 691–698 (2001).
25. Chen, Q., Stajic, J., Tan, S. & Levin, K. BCS–BEC crossover: from high temperature superconductors to ultracold superfluids. *Phys. Rep.* **412**, 1–88 (2005).
26. Randeria, M. & Taylor, E. Crossover from Bardeen–Cooper–Schrieffer to Bose–Einstein condensation and the unitary Fermi gas. *Annu. Rev. Condens. Matter Phys.* **5**, 209–232 (2014).
27. Schrieffer, J. R., Scalapino, D. J. & Wilkins, J. W. Effective tunneling density of states in superconductors. *Phys. Rev. Lett.* **10**, 336–339 (1963).
28. McMillan, W. L. & Rowell, J. M. Lead phonon spectrum calculated from superconducting density of states. *Phys. Rev. Lett.* **14**, 108–112 (1965).

29. Lee, J. et al. Interplay of electron–lattice interactions and superconductivity in $Bi_2Sr_2CaCu_2O_{8+\delta}$. *Nature* **442**, 546–550 (2006).
30. Niestemski, F. C. et al. A distinct bosonic mode in an electron-doped high-transition-temperature superconductor. *Nature* **450**, 1058–1061 (2007).
31. Chi, S. et al. Scanning tunneling spectroscopy of superconducting LiFeAs single crystals: evidence for two nodeless energy gaps and coupling to a bosonic mode. *Phys. Rev. Lett.* **109**, 087002 (2012).
32. Shan, L. et al. Evidence of a spin resonance mode in the iron-based superconductor $Ba_{0.6}K_{0.4}Fe_2As_2$ from scanning tunneling spectroscopy. *Phys. Rev. Lett.* **108**, 227002 (2012).
33. Zasadzinski, J. F. et al. Correlation of tunneling spectra in $Bi_2Sr_2CaCu_2O_{8+\delta}$ with the resonance spin excitation. *Phys. Rev. Lett.* **87**, 067005 (2001).
34. Ramires, A. & Lado, J. L. Emulating heavy fermions in twisted trilayer graphene. *Phys. Rev. Lett.* **127**, 026401 (2021).
35. Carbotte, J. P. Properties of boson-exchange superconductors. *Rev. Mod. Phys.* **62**, 1027–1157 (1990).
36. Song, C.-L. & Hoffman, J. E. Pairing insights in iron-based superconductors from scanning tunneling microscopy. *Curr. Opin. Solid State Mater. Sci.* **17**, 39–48 (2013).
37. Scalapino, D. J., Schrieffer, J. R. & Wilkins, J. W. Strong-coupling superconductivity. I. *Phys. Rev.* **148**, 263–279 (1966).
38. Yu, G., Li, Y., Motoyama, E. M. & Greven, M. A universal relationship between magnetic resonance and superconducting gap in unconventional superconductors. *Nat. Phys.* **5**, 873–875 (2009).
39. Anderson, P. W. & Ong, N. P. Theory of asymmetric tunneling in the cuprate superconductors. *J. Phys. Chem. Solids* **67**, 1–5 (2006).
40. Eschrig, M. & Norman, M. R. Effect of the magnetic resonance on the electronic spectra of high-T_c superconductors. *Phys. Rev. B* **67**, 144503 (2003).

Publisher's note Springer Nature remains neutral with regard to jurisdictional claims in published maps and institutional affiliations.

© The Author(s), under exclusive licence to Springer Nature Limited 2022

Methods

Device fabrication

Similarly to our previous STM measurements on twisted graphene bilayers[8,13,16], the device was fabricated using the polydimethylsiloxane (PDMS)-assisted stack-and-flip technique with about 30-nm hexagonal boron nitride and monolayer graphene. The flakes were exfoliated on silicon dioxide and identified optically. We used a poly(bisphenol A carbonate) (PC)/PDMS stamp to pick up the hexagonal boron nitride at 90 °C, and tear and twist graphene layers at 40 °C. The PC film with the stack was then peeled off and transferred onto another clean PDMS, with the MATTG side facing the PDMS. The PC film was dissolved in *N*-methyl-2-pyrrolidone, followed by cleaning with isopropyl alcohol. The final PDMS was kept in vacuum for several days. The stack on it was then transferred onto a chip with a graphite back gate and gold electrodes. Finally, MATTG was connected to the electrodes by another graphite flake.

STM measurements

The STM measurements were performed in a Unisoku USM1300J STM/AFM system using a platinum/iridium tip as in our previous studies on bilayers[8,13,16]. All reported features were observed with many (more than ten) different microtips. Unless specified otherwise, the parameters for the dI/dV spectroscopy measurements were V_{Bias} = 100 mV and I = 1 nA, and the lock-in parameters were modulation voltage V_{mod} = 0.2–1 mV and frequency f = 973 Hz. The piezo scanner was calibrated on a Pb(110) crystal by matching the lattice constant and verified by measuring the distance between carbon atoms. The twist-angle uncertainty was approximately ±0.01, and was determined by measuring moiré wavelengths from topography. Filling-factor assignment was performed by taking Landau fan diagrams as discussed previously[13] or by identifying features corresponding to full-filling and CNP LDOS suppression[8] in datasets where magnetic-field dependence was not studied. The deviations between the two methods in assigning filling factors are typically within a 5% margin.

Correcting zero-bias offsets

Occasionally, in some of the measurements focused on resolving the details of the superconducting gap, we observed drifts of the zero-bias voltage (of the order of about 100 μV). These offsets were detected by noticing the existence of a finite current when V_{Bias} = 0 mV is applied. We attributed these offsets to the electronic drifts in our STM system and noted that similar offsets have been observed previously in similar setups (see, for example, the discussion in the supplementary information of ref. [41] or ref. [42]). The offsets were corrected by attributing real 'zero' bias to the point where the tunnelling current becomes zero and shifting the spectra accordingly.

Band-flattening in MATTG. As in twisted bilayers in MATTG, we also observed the band-flattening effect. This effect originates from the inhomogeneous real-space charge distribution associated with different energy eigenstates: the majority of the weight of the flat-band states (including those near the VHS) are spatially located on the AAA moiré sites, whereas the additional Dirac cones and flat-band states in the immediate vicinity of the γ point are more uniformly distributed (Extended Data Fig. 2). Electrostatic doping thereby gives rise to a Hartree potential that modifies the band structure in a manner that promotes charge uniformity throughout the unit cell. In twisted bilayer graphene, it was found[16] that this potential generates additional band deformations[43–46]. Our simulations capture a similar band renormalization in MATTG accompanied by a displacement of the additional Dirac cones away from the flat bands[14,15] (Fig. 2b). Both effects—band deformations (Fig. 2e–h) and the relative Dirac cone shift—are clearly confirmed in our measurements. Importantly, the position of the Dirac point obtained by tracking the zeroth LL (Fig. 2c, d) falls within ±50 meV depending on the exact doping; it resides below the lower flat-band VHS at υ = +4, but moves above the upper flat-band VHS at υ = −4. Finally, we note that the LLs from the Dirac cones appear unaltered by the cascade of phase transitions in the flat bands, suggesting that the flat-band and Dirac sectors are not strongly coupled by interactions[47].

Point contact spectroscopy. In addition to tunnelling spectroscopy and the detection of superconducting gaps, we performed point contact spectroscopy (PCS) in search for the process of Andreev reflection, which would provide independent evidence for superconductivity in our samples. These measurements were performed by significantly reducing the tip-to-sample distance to reach the point-contact regime (with tip–sample resistance in the 10–100 kΩ range). We performed V_{Gate}-dependent PCS measurements on MATTG and identified a range of filling factors showing the enhanced conductance signal around V_{Bias} = 0 mV. This PCS enhancement near zero bias occurs only in the limiting range of filling factors where the tunnelling gap accompanied by coherence peaks is also observed. Importantly, the PCS signal further distinguishes the filling factor range corresponding to correlated insulators (located at the immediate vicinity of υ = −2) where conductance at V_{Bias} = 0 mV is significantly reduced (compared with conductance at V_{Bias} = 1 mV) from the broader region (observed in the approximate range $-3 < \upsilon < -2.2$) where enhanced zero-bias conductance is identified. Moreover, the zero-bias enhancement of the PCS signal diminishes when a finite out-of-plane magnetic field is applied (Fig. 1c) and at elevated temperature (Fig. 1d, e). All observed PCS features in the filling factor range $-3 < \upsilon < -2.2$ are fully consistent with the process of Andreev reflection and are qualitatively similar to findings reported for twisted bilayer graphene[5].

Additional discussion on the peak–dip–hump structure. The observed peak–dip–hump structure and the fact that, in the V-shaped region, $\Omega/(2\Delta)$ anticorrelates with the gap is in line with trends seen in cuprates and iron-based compounds[29,30,32,33,38]. Importantly, this ratio is bounded to be and less than 1. As such, it is compatible with electronic mechanisms (see refs. [14,48] for examples of such mechanisms). It is noted that electronic excitations with energy above 2Δ would become rapidly damped by the particle–hole continuum, unlike for phonon modes. However, although suggestive, this line of argument cannot rule out phonon-mediated superconductivity[49,50]. It may be, for example, that the observed structure originates from low-energy phonons and that even higher phonon branches are present but not resolvable[51]. Finally, dip–hump features are also associated with proximate competing orders as discussed in relation to the cuprates[52–54], which may be present in twisted bilayer graphene[55] and possibly MATTG.

Data availability

The data that support the findings of this study are available from the corresponding author on reasonable request.

41. Wang, D. et al. Evidence for Majorana bound states in an iron-based superconductor. *Science* **362**, 333 (2018).
42. Chen, M. et al. Discrete energy levels of Caroli-de Gennes-Matricon states in quantum limit in $FeTe_{0.55}Se_{0.45}$. *Nat. Commun.* **9**, 970 (2018).
43. Guinea, F. & Walet, N. R. Electrostatic effects, band distortions, and superconductivity in twisted graphene bilayers. *Proc. Natl Acad. Sci. USA* **115**, 13174–13179 (2018).
44. Rademaker, L., Abanin, D. A. & Mellado, P. Charge smoothening and band flattening due to Hartree corrections in twisted bilayer graphene. *Phys. Rev. B* **100**, 205114 (2019).
45. Goodwin, Z. A. H., Vitale, V., Liang, X., Mostofi, A. A. & Lischner, J. Hartree theory calculations of quasiparticle properties in twisted bilayer graphene. *Electron. Struct.* **2**, 034001 (2020).
46. Caldero´n, M. J. & Bascones, E. Interactions in the 8-orbital model for twisted bilayer graphene. *Phys. Rev. B* **102**, 155149 (2020).
47. Christos, M., Sachdev, S. & Scheurer, M. S. Correlated insulators, semimetals, and superconductivity in twisted trilayer graphene. *Phys. Rev. X* **12**, 021018 (2022).
48. Khalaf, E., Chatterjee, S., Bultinck, N., Zaletel, M. P. & Vishwanath, A. Charged skyrmions and topological origin of superconductivity in magic-angle graphene. *Sci. Adv.* **7**, eabf5299 (2021).

49. Lewandowski, C., Chowdhury, D. & Ruhman, J. Pairing in magic-angle twisted bilayer graphene: role of phonon and plasmon umklapp. *Phys. Rev. B* **103**, 235401 (2021).
50. Chou, Y.-Z., Wu, F., Sau, J. D. & Das Sarma, S. Correlation-induced triplet pairing superconductivity in graphene-based moiré systems. *Phys. Rev. Lett.* **127**, 217001 (2021).
51. Choi, Y. W. & Choi, H. J. Dichotomy of electron–phonon coupling in graphene moiré flat bands. *Phys. Rev. Lett.* **127**, 167001 (2021).
52. Reznik, D. et al. Electron–phonon coupling reflecting dynamic charge inhomogeneity in copper oxide superconductors. *Nature* **440**, 1170–1173 (2006).
53. Le Tacon, M. et al. Inelastic X-ray scattering in $YBa_2Cu_3O_{6.6}$ reveals giant phonon anomalies and elastic central peak due to charge-density-wave formation. *Nat. Phys.* **10**, 52–58 (2014).
54. Gabovich, A. M. & Voitenko, A. I. Charge density waves as the origin of dip–hump structures in the differential tunneling conductance of cuprates: the case of *d*-wave superconductivity. *Physica C* **503**, 7–13 (2014).
55. Cao, Y. et al. Nematicity and competing orders in superconducting magic-angle graphene. *Science* **372**, 264–271 (2021).

Acknowledgements We acknowledge discussions with F. von Oppen, G. Refael, Y. Peng and A. Yazdani. This work was primarily supported by the Office of Naval Research (grant number N142112635); the National Science Foundation (grant number DMR-1753306); and the Army Research Office under grant award W911NF17-1-0323. Nanofabrication efforts were in part supported by Department of Energy DOE-QIS programme (DE-SC0019166) and National Science Foundation (grant number DMR-2005129). S.N.-P. acknowledges support from the Sloan Foundation. J.A. and S.N.-P. also acknowledge support from the Institute for Quantum Information and Matter, an NSF Physics Frontiers Center with support of the Gordon and Betty Moore Foundation through grant GBMF1250; C.L. acknowledges support from the Gordon and Betty Moore Foundation's EPiQS Initiative, grant GBMF8682. A.T. and J.A. are grateful for the support of the Walter Burke Institute for Theoretical Physics at Caltech. H.K. and Y.C. acknowledge support from the Kwanjeong fellowship.

Author contributions H.K. and Y.C. fabricated samples with the help of Y.Z. and R.P., and performed STM measurements. H.K., Y.C. and S.N.-P. analysed the data. C.L. and A.T. provided the theoretical analysis supervised by J.A. S.N.-P. supervised the project. H.K., Y.C., C.L., A.T., J.A. and S.N.-P. wrote the manuscript with input from the other authors.

Competing interests The authors declare no competing interests.

Additional information

Supplementary information The online version contains supplementary material available at https://doi.org/10.1038/s41586-022-04715-z.

Correspondence and requests for materials should be addressed to Stevan Nadj-Perge.

Peer review information *Nature* thanks Iván Brihuega and the other, anonymous, reviewer(s) for their contribution to the peer review of this work.

Reprints and permissions information is available at http://www.nature.com/reprints.

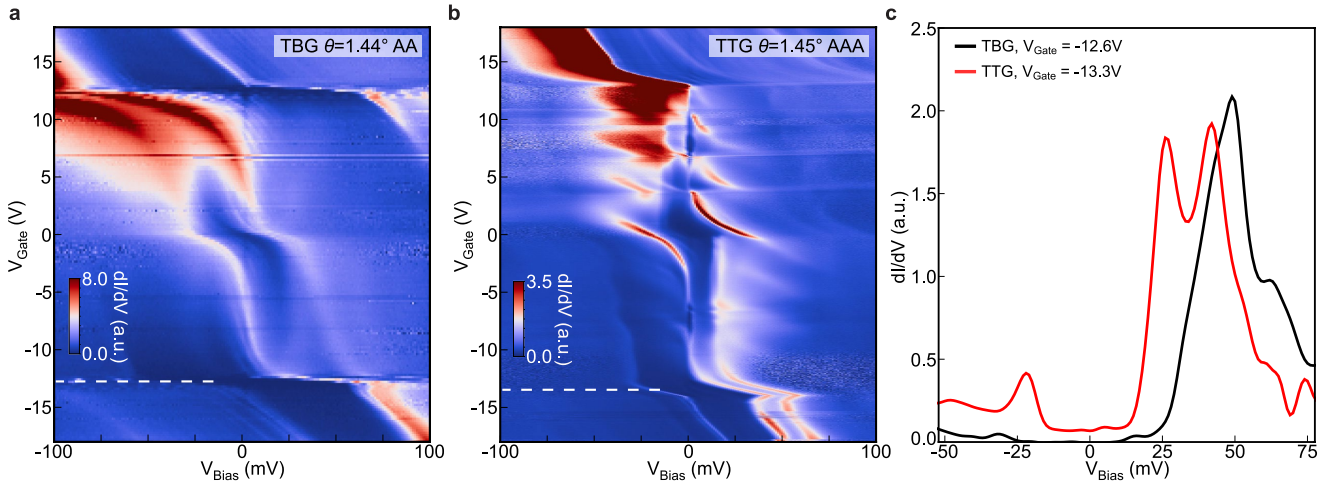

Extended Data Fig. 1 | Spectroscopy of twisted bilayer and twisted trilayer graphene. a, Point spectra of twisted bilayer graphene (TBG) on an AA site at a twist angle $\theta = 1.44°$, from a bilayer region found in the same sample. **b**, Point spectra of twisted trilayer graphene (TTG) on an AAA site at a twist angle $\theta = 1.45°$. Unlike TBG at the similar angle, signatures of correlations, such as enhancement of VHS separations at charge neutrality and cascade of flavour symmetry breaking, are observed. **c**, Linecuts taken from **a**, **b** around $\upsilon = -4$ (white dashed lines). While the $dI/dV \sim$ LDOS between the flat bands and the remote band is zero for TBG, the value is finite for TTG due to the existence of the additional Dirac cones.

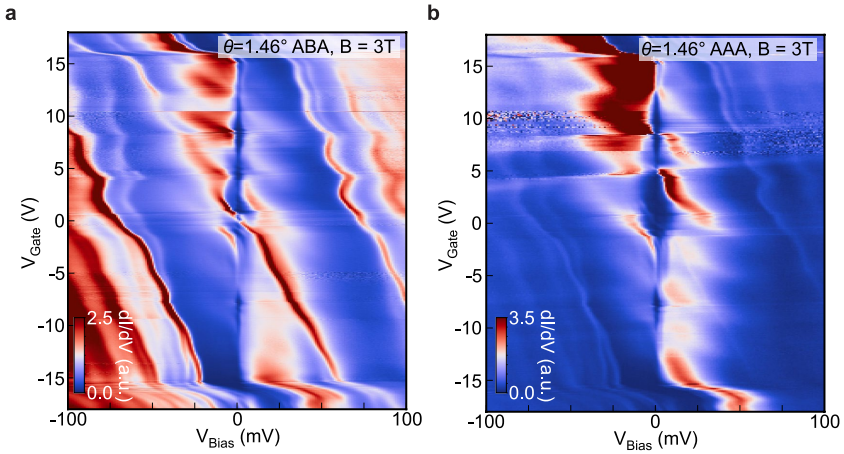

Extended Data Fig. 2 | Comparison between spectra on ABA and AAA sites at finite fields. a, b, Point spectroscopy as a function of V_{Gate} on ABA stacked (**a**, the same as panel Fig. 2d) and on AAA stacked (**b**) region ($B = 3$ T, $\theta = 1.46°$). In comparison, flat bands appear to be more prominent on the AAA site (**b**), while LLs from Dirac-like dispersion and dispersive bands appear more pronounced at ABA site. This is a direct consequence of LDOS from the flat bands being localized on the AAA sites. The LDOS from Dirac-like bands is spatially uniformly distributed.

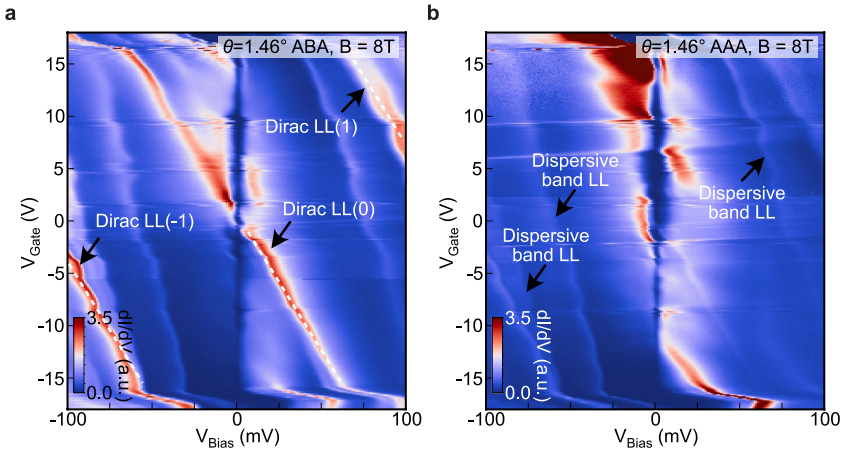

Extended Data Fig. 3 | Distinguishing dispersive band LLs and Dirac band LLs. a, b, Point spectroscopy as a function of V_{Gate} on ABA stacked (**a**) and AAA stacked (**b**) region ($B = 8$ T, $\theta = 1.46°$). Zeroth LL from Dirac dispersion is clearly distinguished from other LLs as it crosses the flat band. Other LLs from Dirac dispersion is distinguished from the dispersive band from being parallel to the zeroth LL as a function of doping. Additional LL is observed at this high magnetic field at $V_{Gate} > 12$ V which is more pronounced at AAA stacked region and can be attributed to second Dirac cone due to finite displacement field present at these V_{Gate}.

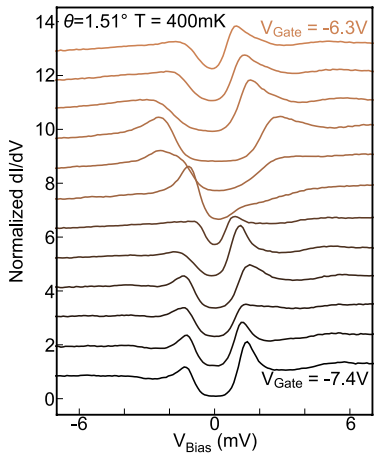

Extended Data Fig. 4 | Spectroscopy near $\nu = -2$. Linecuts taken from Fig. 3a for V_{Gate} ranging from −6.3 V to −7.4 V in 100 mV steps. Starting from top, the observed gap is highly asymmetric and gradually evolves to the more symmetric spectrum on the bottom. Vertical dashed line shows the position of $V_{Bias} = 0$ mV. We interpret that asymmetric gap (brown lines) corresponds to correlated insulator regime, while the symmetric gap (black lines) indicates superconducting regime.

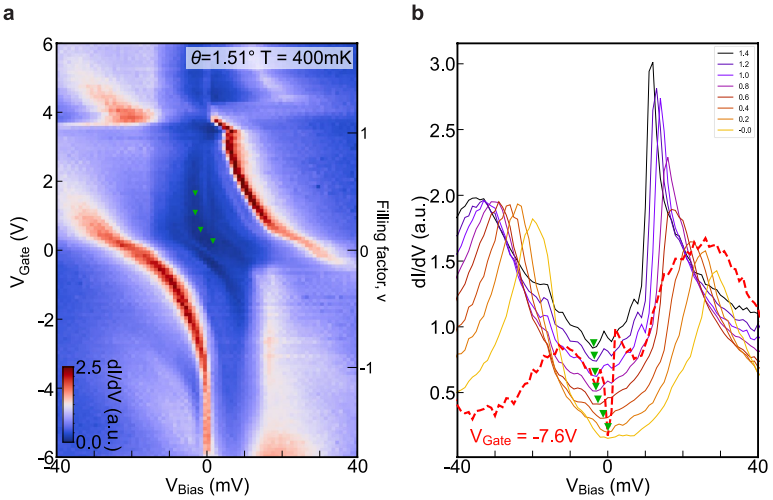

Extended Data Fig. 5 | Spectral features around CNP and their comparison to the superconducting (SC) gap at $\nu \approx -2.1$. a, Zoom-in 2D gate spectroscopy of Fig. 1f in the main text. Green triangles mark the position of LDOS suppression around $V_{Bias} = 0$ mV at multiple V_{Gate}. **b**, Linecuts of (**a**) at $V_{Gate} = 1.4$ V to 0 V as indicated by numbers (in volts) indicated in the legend. Green triangles mark the position of same LDOS suppression in (**a**). Line traces are offset for clarity. Red dashed line is linecut at $V_{Gate} = -7.6$ V from same 2D gate spectroscopy in Fig. 1f of the main text showing the spectrum of SC gap.

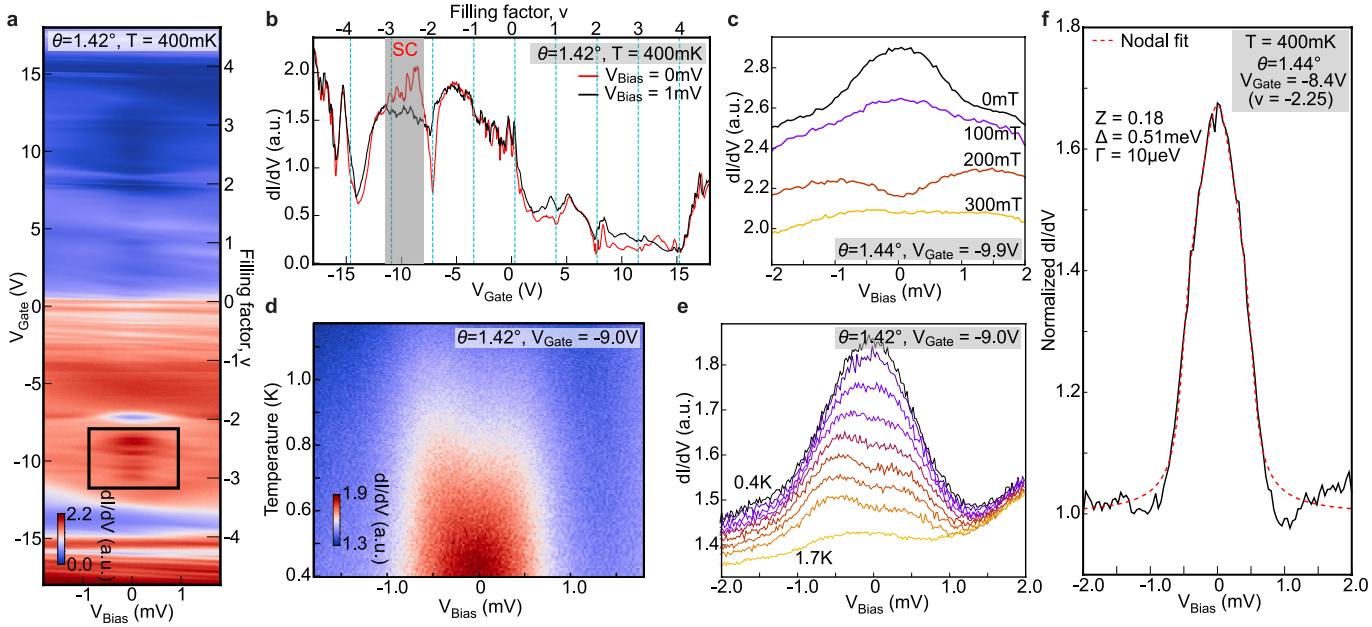

Extended Data Fig. 6 | Andreev reflection signal from point contact spectroscopy of MATTG. a, Point contact conductance (dI/dV) spectroscopy as a function of V_{Gate} at twist angle $\theta = 1.42°$ at $T = 400$ mK. The black box highlights the filling factor range $-3 < \upsilon < -2.2$ where clear signatures of the we Andreev reflection are observed. **b**, Linecut of point contact dI/dV as a function of V_{Gate}. Grey region marks the filling factor range where Andreev reflection signal is observed. **c**, PCS dI/dV spectra for 4 different perpendicular magnetic field at twist angle $\theta = 1.44°$. Lines are offset for clarity. **d**, PCS dI/dV conductance as a function of temperature and V_{Bias}. **e**, Linecuts from **d** for $T = 0.4 - 1.1$ K and the additional trace at $T = 1.7$ K showing the suppression of the Andreev reflection. These temperatures are slightly smaller (by a factor of 1.5–2) compared to the temperature scales where coherence peaks get completely suppressed.

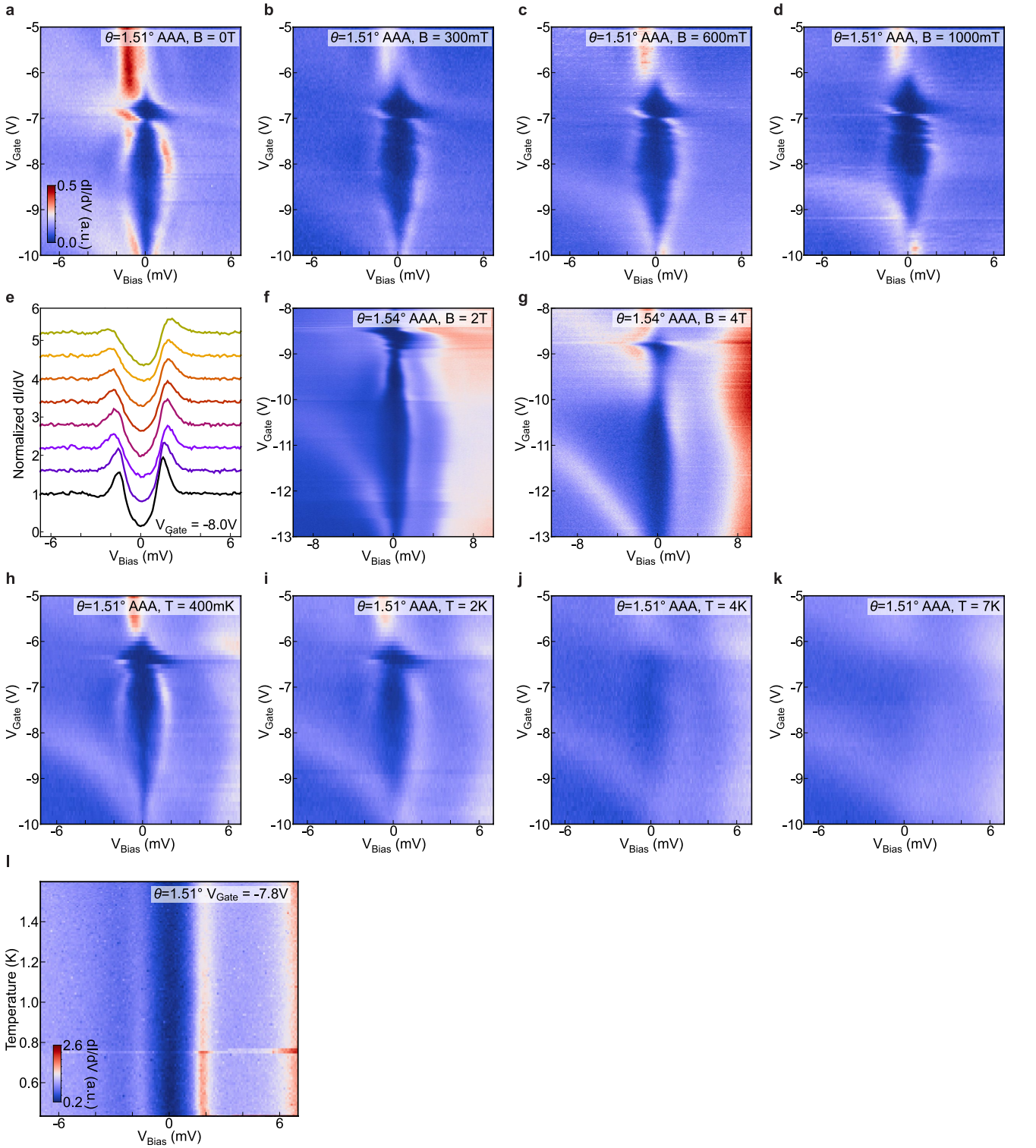

Extended Data Fig. 7 | Additional datasets showing magnetic field and temperature dependence of spectroscopic gap in the $-3 < \nu < -2$ range. **a**–**d**, Point spectroscopy as a function of V_{Gate} at twist angle of $\theta = 1.51°$ at magnetic field $B = 0$ T (**a**), $B = 300$ mT (**b**), B = 600 mT (**c**), $B = 1$ T (**d**). **e**, Line traces showing magnetic field dependence for $V_{Gate} = -7.8$ V (U-shaped regime). Colour coding corresponds to magnetic field $B = 0$, 0.1, 0.2, 0.3, 0.4, 0.4, 0.8, 1 T. Plots are offset for clarity. **f**, **g**, Gate spectroscopy measured at $B = 2$ T (**f**) and $B = 4$ T (**g**), for $\theta = 1.54°$ featuring gapped spectrum persisting $B \gtrsim 4$ T (data taken at different point compared to **a**–**e**). **h**–**k**, Gate spectroscopy taken at different temperatures $T = 400$ mK (**h**), $T = 2$ K (**i**), $T = 4$ K (**j**), $T = 7$ K (**k**). **i**, Point spectroscopy measured as a function of V_{Bias} and temperature at the same point as (**h**–**k**) for $V_{Gate} = -7.8$ V.

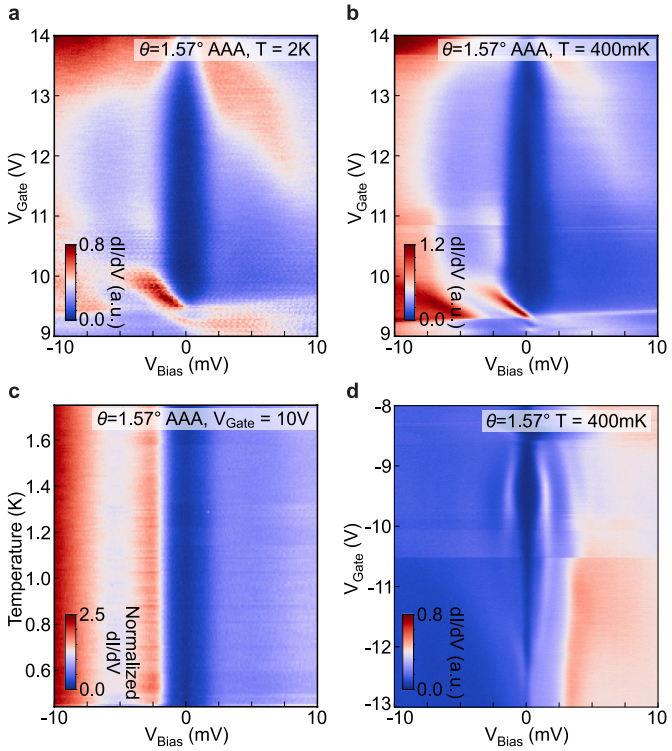

Extended Data Fig. 8 | Spectroscopic gap in the +2 < ν < +3 range. **a**, Tunnelling conductance spectroscopy at twist angle of $\theta = 1.57°$ on AAA stacked region at $T = 2$ K showing well-developed gapped region on the electron-side. **b**, Spectroscopy measured at the same region at $T = 400$ mK. **c**, Spectroscopy as a function of temperature at the same point as (**a**, **b**) for $V_{Gate} = 10$ V. **d**, Spectroscopy focusing on hole doping taken with the same micro-tip. While the spectrum for hole doping (**d**) shows clear coherence peaks and dip–hump structures these features are absent for the gap on the electron-side. We speculate that for electron doping, the coherence peaks are suppressed even at our base temperature ($T = 400$ mK), which would suggest that the observed gap corresponds to pseudogap phase. However, further investigation is needed to confirm this scenario and rule out other possible origins.

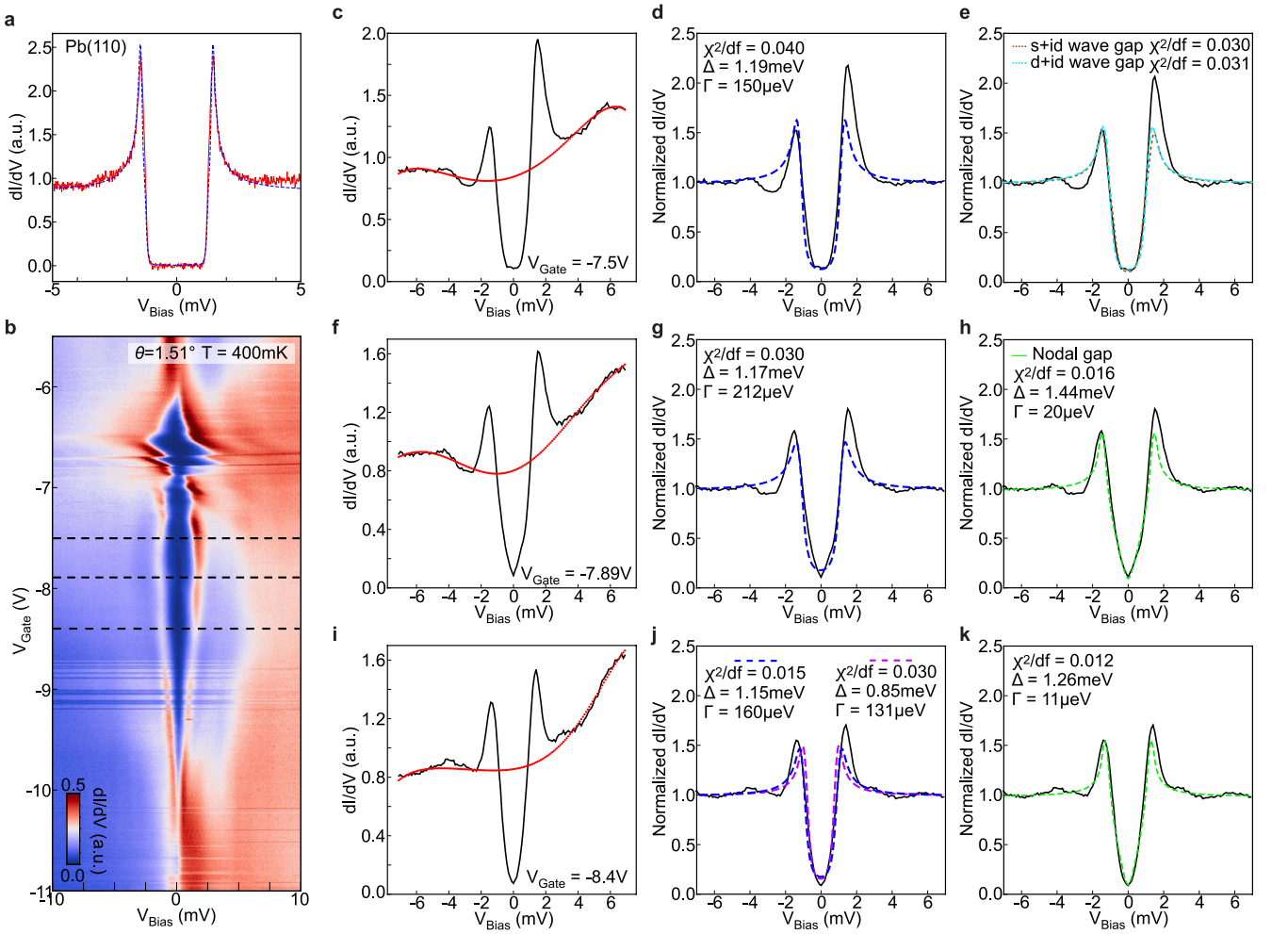

Extended Data Fig. 9 | Normalization of tunnelling conductance and fitting. a, Tunnelling conductance measured on Pb (110) surface at $T = 400$ mK showing superconducting gap. Blue dashed line is Dynes formula fit with two gaps with following parameters, $\Delta_1 = 1.42$ meV, $\Delta_2 = 1.26$ meV, $\Gamma = 10$ μeV, $T = 400$ mK used to obtain the base temperature. **b**, Same data as Fig. 3a showing larger V_{Bias} range. Black dashed lines mark gate voltages $V_{Gate} = -7.5$, -7.89, -8.4 V with the corresponding line traces shown in subsequent panels. **c**, Line cut in the U-shaped regime ($V_{Gate} = -7.5$ V). Red dotted line is polynomial fitting curve obtained as described in Supplementary Information 4. **d**, Normalized data obtained by dividing the raw data (black line in **c**) by polynomial fit (red line in **c**). Blue line is Dynes formula fit with isotropic gap. **e**, Same data as **d** with Dynes formula fits using different types of the pairing gap symmetry: $s + id$ pairing gap with $\Delta_s = 0.88$ meV, $\Delta_d = 1.10$ meV, $\Gamma = 135$ eV (brown); $d + id$ pairing gap with $\Delta_{d1} = 0.85$ meV, $\Delta_{d2} = 1.35$ meV, $\Gamma = 135$ eV (cyan). **f**, In the V-shaped regime ($V_{Gate} = -7.89$ V). **g**, Normalized data from **f** and Dynes formula fit using an isotropic gap (blue). **h**, Normalized data from **f** with Dynes formula fits using a nodal gap with $\Delta = 1.44$ meV (green). **i**, Another linecut in the V-shaped regime ($V_{Gate} = -8.4$ V). **j**, Normalized data from **i** and Dynes formula fit using an isotropic gap (blue, purple). **k**, Normalized data from **i** and Dynes formula fits green line is nodal gap with $\Delta = 1.26$ meV.

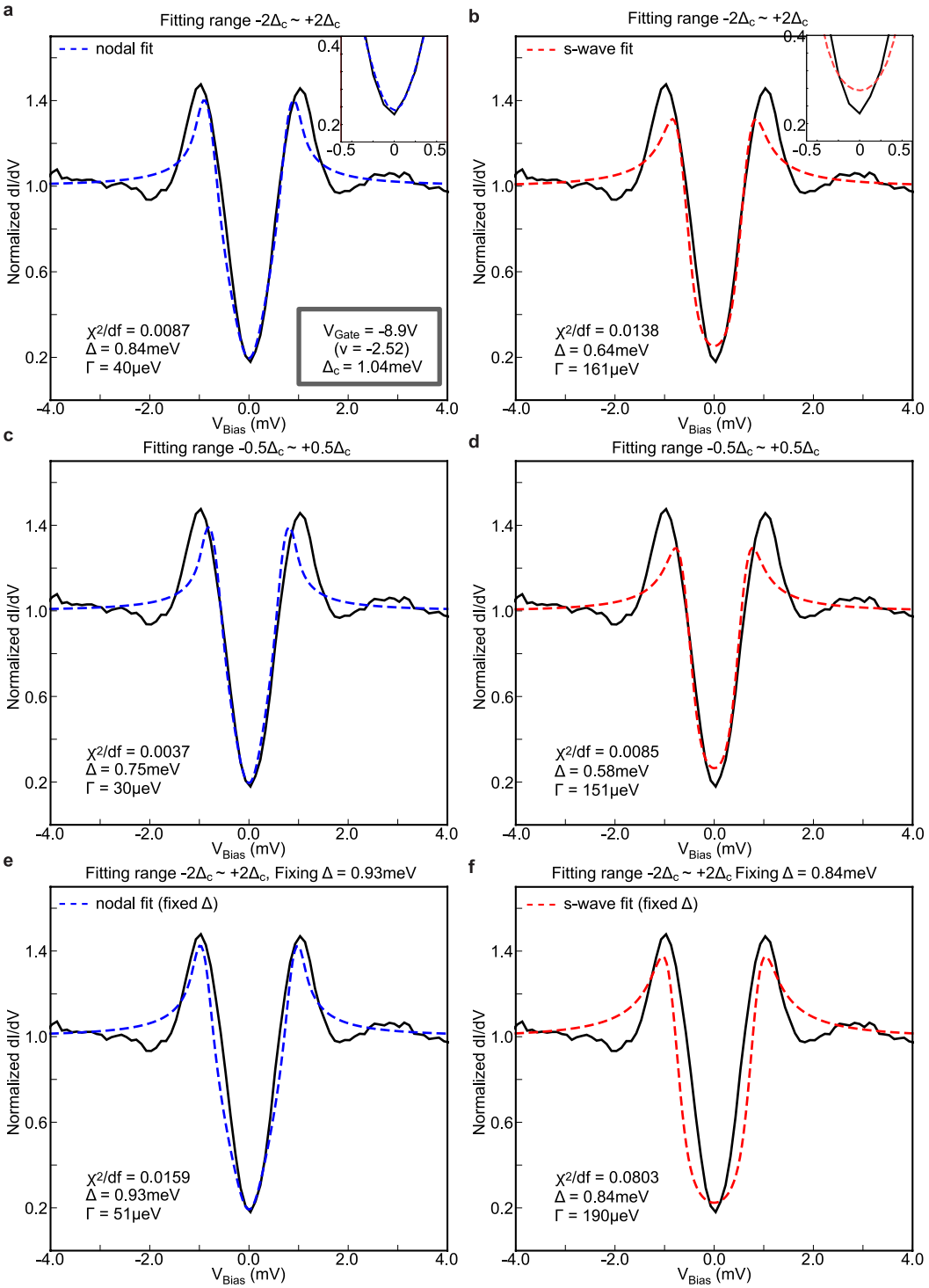

Extended Data Fig. 10 | Comparing Nodal and s-wave pairing symmetry fit in the V-shaped region. a, **b**, Normalized dI/dV spectrum and its nodal (**a**) and *s*-wave (**b**) fit at $V_{Gate} = -8.4$ V. Fit parameters Δ and Γ are obtained by performing least square method within $-2\Delta_c$ to $2\Delta_c$ V_{Bias} range where Δ_c is 1.04 meV defined by half of the separation between coherence peaks. Nodal fit from $1\Delta_c$ to $1\Delta_c$ shows almost The inset is a zoom-in around $V_{Bias} = 0$ mV where the deviation between the two is largest. **c**, **d**, Nodal (**c**) and *s*-wave (**d**) fit for same data in (**a**, **b**) with fixed Δ so that the position of the coherence peak from the fit curve matches to the position of the coherence peak in the data. Fit parameter Γ is obtained by fitting within $-2\Delta_c$ to $2\Delta_c$. *S*-wave fit shows even larger deviation from the data in this case. **e**, **f**, Nodal (**e**) and s-wave(**f**) fit for the same data in (**a**, **b**) where fit parameters Δ and Γ are obtained within reduced V_{Bias} range $-0.5\Delta_{cc}$ to $0.5\Delta_c$. All χ^2/df values are calculated within the V_{Bias} range where least square method is performed.

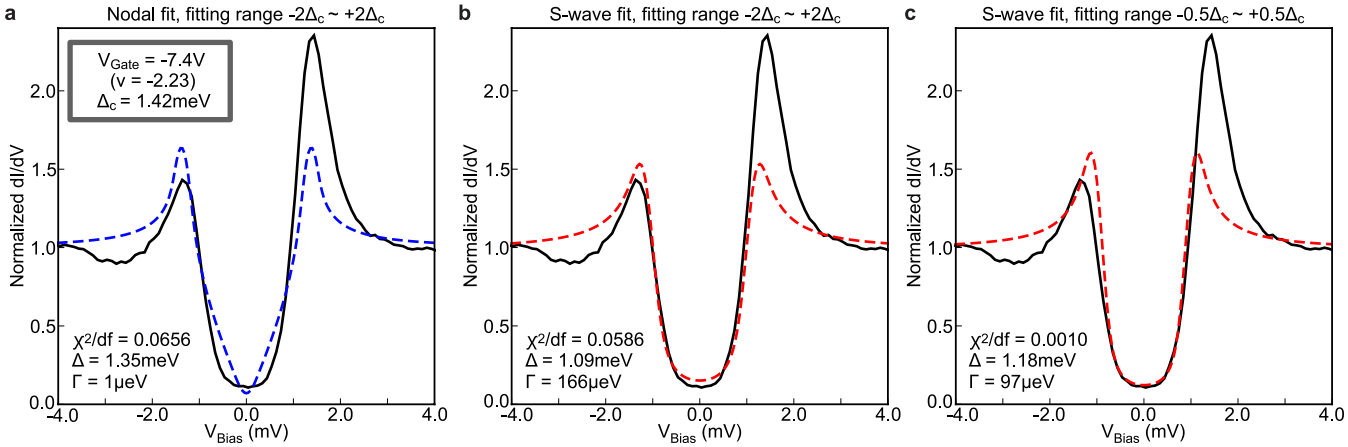

Extended Data Fig. 11 | Dynes formula fit to nodal and *s*-wave gap in the U-shaped region. a, **b**, Normalized dI/dV spectrum and its nodal fit (**a**) and *s*-wave fit (**b**) at $V_{Gate} = -7.4$ V. Fit parameters Δ and Γ are obtained by performing least square optimization in $-2\Delta_c$ to $2\Delta_c$ range of V_{Bias}, where $\Delta_c = 1.2$ meV. **c**, Same data as (**a**, **b**) with fit parameters obtained from reduced V_{Bias} range $-0.5\Delta_c$ to $0.5\Delta_c$. This gives better fit around $V_{Bias} = 0$ meV. χ^2 values are calculated within the V_{Bias} range where least square optimization is performed.